Springer

KSME

Journal of Mechanical Science and Technology 32 (12) (2018) 5711~5721
www.springerlink.com/content/1738-494x(Print)/1976-3824(Online)
DOI 10.1007/s12206-018-1118-4

The evaluation of numerical methods for determining the efficiency of Tesla turbine operation †

Krzysztof Rusin*, Włodzimierz Wróblewski and Sebastian Rulik

Silesian University of Technology, 44-100 Gliwice, Poland

(Manuscript Received May 8, 2018; Revised July 9, 2018; Accepted July 30, 2018)

Abstract

The Tesla turbine operation is based on the use of tangential stresses arising from the fluid viscosity and turbulence and from the phenomenon of the fluid adhesion to the surface it flows past. The paper presents a description and testing of the Tesla turbine model, pointing to the impact of the applied turbulence models on the prediction of the Tesla turbine operating conditions. Non-stationary simulations are performed using the Ansys CFX 18 commercial code. The following turbulence models are analysed: the RNG k-ε, the k-ω SST and the SST-SAS in two variants of time and space discretization. The flow field structures and the flow unsteadiness occurring in the gaps between the rotor discs are described. The distribution of power unit arising on the discs is determined and the predictions as to the power generated by the turbine coming from numerical analysis and preliminary experimental investigations are compared. A comparison of efficiency estimation is made using different methods.

Keywords: Bladeless turbine; CFD simulation; Tesla turbine; Turbine efficiency evaluation; Turbulence models

1. Introduction

The Tesla turbine, also known as the bladeless turbine or the boundary layer turbine, was built by Nikola Tesla in 1906. It was patented in 1915 [1]. Though successful at the beginning, Tesla soon encountered obstacles that at that time were insurmountable. As no appropriate materials capable of withstanding high stresses arising in discs (estimated by Tesla at the level of 350 MPA [2]) were available, the works on the turbine development were discontinued. At present, due to the progress in design materials, the Tesla turbine has again become the subject of research.

Although the turbine structure is relatively simple, the flow in it is rather complex. The fluid is fed to the rotor at an appropriate angle by a supply system made of nozzles. It is in the nozzles where the fluid is expanded, which involves a rise in its velocity. The optimal geometry of the nozzles is extremely important in terms of the turbine performance because the losses occurring there are the main causes of the drop in efficiency [3, 4]. The medium velocity at the nozzle outlet often exceeds the speed of sound, which may generate shock waves [5]. Being strongly non-isentropic phenomena, shock waves also involve a drop in the turbine efficiency. Moreover, propagating in the rotor, they favour flow disturbance and incidents of the fluid jet separation [6]. Another essential factor that affects the turbine efficiency is the ratio between pressure values at the inlet and at the outlet of the nozzle. If the fluid in the nozzle expands to a pressure level exceeding the value prevailing beyond the supply system, expansion and secondary compression may occur [7]. These are entropy-generating processes and as such – they cause a decrease in efficiency. Having expanded in the nozzle, the fluid is directed to the region of the rotor composed of flat discs mounted on a shaft. Due to adhesion forces between the particles of the discs and the fluid, the latter adheres to the disc walls. The transfer of energy from the working medium to the disc occurs owing to the moment diffusion, which is an effect of the fluid viscosity. The layers of the jet moving more slowly absorb particles from the faster layers of the fluid and thus increase their momentum. Being strongly bound by intermolecular forces with the fluid first layer, the disc also increases its momentum, which makes the rotor rotate. The fluid elements move spirally in relation to the outlets located close to the rotor axis. The outlet system geometry and the method in which the working medium is extracted from the turbine also have an effect on the turbine total efficiency [4, 8]. The main problems that may result in a drop in efficiency is an abrupt change in the fluid outflow direction and its high outlet velocity increasing the kinetic loss.

The Tesla turbine has a number of advantages [9, 10]. The most important is the unsophisticated structure, which means

*Corresponding author. Tel.: +48 322371425
E-mail address: krzysztof.rusin@polsl.pl
† Recommended by Associate Editor Donghyun You

low costs of manufacture. Consequently, the profitability of an installation with a bladeless expander is greater. Corrosion resistance and the flexibility of choice of the working medium [11] are of particular importance in the case of an ORC installation [12, 13]. One of the main problems in conventional turbines used in such installations is condensation, which is the main cause of erosion [14]. The fact that the flow in the Tesla turbine is tangential to the surface substantially decreases erosion caused by solid particles or condensate droplets. As a result, the risk of the turbine failure is reduced. The possibility of applying bladeless turbines in ORC systems has been a frequent subject of research. Carey [15] analysed a 4 kW solar cogeneration system. The analysis results prove that, if appropriate flow parameters are kept, it is possible to achieve the turbine efficiency at the level of 80 %. Kim and Yoon [11] also investigated the possibility of using a bladeless turbine in a cogeneration system supplied with waste heat. In their experiment, they achieved the power value of 4.25 kW at the efficiency of 26 %. Lampart et al. [16] tested the operating conditions of a micro Tesla turbine in a cogeneration system producing 20 kW of heat. The obtained results prove that in terms of efficiency bladeless turbines may equal turbines with blades in installations with a low-boiling fluid. Song et al. [17] tested the impact of the ORC installation working medium on the Tesla turbine performance. Of all the considered fluids, the highest efficiency at the level of 36.6 % was achieved using the R245ca medium. Another essential advantage is the flow reversibility. Miller et al. [18] proposed using a disc pump, based on the same effects as the Tesla turbine, as a blood flow device. It is proved that the Tesla pump can produce physiological pulsations in pressure and, in terms of flow parameters, it equals other pumps intended for this purpose. If its supply and exhaust systems are modified slightly, the Tesla turbine can operate in the mode of a compressor or pump. This means the potential for use in compressed air energy storage (CAES) systems [19, 20].

The Tesla turbine main weakness is low efficiency. This is due to a number of factors, but the most essential are [10, 21]: The pressure ratio, the spacing between the discs, the disc surface roughness, the fluid type and the rotor rotational speed. The main culprit here are the losses arising in the supply and in the exhaust system [4]. Hoya and Guha [22] used the static pressure loss to determine the efficiency of supply nozzles. The friction factor, which expresses friction-related energy losses, was 10 times higher in the Tesla turbine than in the gas turbine. Guha and Smiley [23] proposed a new geometrical solution that enables a substantial reduction in such losses. Li et al. [24] found in their experiment that the rotor rotational speed had a significant impact on losses in the exhaust system.

Some design solutions of the turbine elements seem to be far from optimal and need to be improved. Numerical simulations can be applied for this purpose, but they require a numerical model that will take account of the most important phenomena and processes occurring in the turbine. This paper presents an assessment of the impact of the selected turbulence model on the calculation results. Three turbulence models are presented and the differences in the parameter distributions are compared. A comparison is also made of the turbine power as the global parameter defining the turbine performance. 5 methods of efficiency prediction based on different assumptions are also presented.

2. Computational model

2.1 Geometrical and mathematical model

The numerical simulations were performed using the Ansys 18.0 commercial software package. The geometrical model reflected the dimensions of a real turbine, the rotor of which is composed of 5 discs with diameter D = 73 mm; the spacing between the discs totals b = 1.5 mm. The model takes account of the turbine half: both sides of two discs and one side of the third. This simplification shortens the computation time substantially and poses smaller requirements as to computer resources, but it does not affect the prediction of the turbine operating conditions. The computational domain area (marked in frame) is presented in Fig. 1. Fig. 2 presents the geometrical model with the most important boundary conditions.

The supply system is composed of a cylindrical chamber with the diameter of 6 mm. The fluid flows from the chamber into the rotor through orifices with the diameter of 1.8 mm. The model takes account of two supply orifices. The supply system chamber is located between the nozzle and the rotor. Additionally, the model takes account of the clearance of 1 mm between the rotor tip and the turbine casing.

The area of the inter-disc gaps is a stationary domain with rotating walls. The *no-slip wall* condition is assumed on the surface of the walls. The domain of the spacers, with a characteristic spiral shape of the arms, is assumed as rotating. The aim of the spacers is to hold constant distance during operating of the turbine. Their spiral shape is supposed to facilitate and organize outflow from the rotor. Moreover, due to pressure gradient in the rotor, pressure force is also acting on the arms of the spacer and contribute to the generation of power. Depending on the flow parameters, increase in power may be up to 1.5 %. More detailed discussion on this subject is presented in Ref. [8]. The domains of the spacers and of the gaps between the discs are connected to each other using the *frozen rotor interface*. The fluid leaves the rotor through 5 orifices with the diameter of 7.5 mm, located 10 mm away from the axis. The exhaust system is composed of two chambers and 4 cylindrical connectors in between.

A duct with the diameter of 11 mm and the length of 20 mm is connected to the second chamber to carry the medium out directly into the environment. The exhaust system is stationary and connected to the rotating domain of the spacers by means of the *frozen rotor interface*.

The conservation equations are solved numerically using a high resolution scheme adopted for spatial discretization. Time discretization is carried out using the second-order backward Euler transient scheme. Dynamic viscosity is an

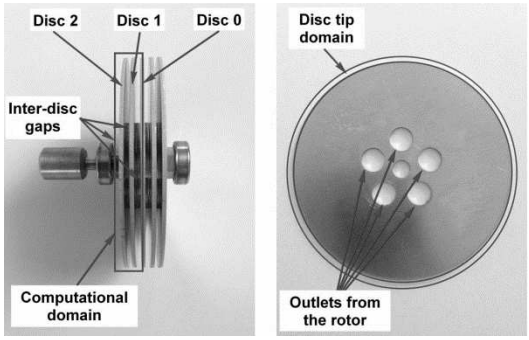

Fig. 1. Computational domain area.

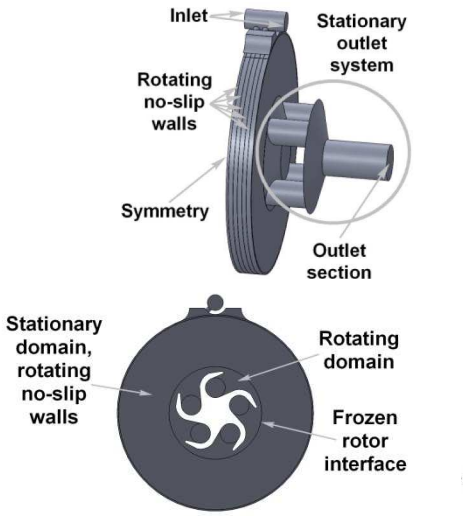

Fig. 2. Basic boundary conditions of the numerical model.

essential parameter. By determining tangential stresses in the fluid, it has a direct impact on the power generated by the Tesla turbine. Due to considerable changes in the flow temperature between the discs, its impact on the laminar viscosity value is taken into consideration. In the numerical model, viscosity as a function of the fluid temperature is determined using the Sutherland formula [25]:

$$\mu = \mu_{ref}\left(\frac{T}{T_{ref}}\right)^{3/2}\frac{T_{ref}+T_S}{T+T_S} \tag{1}$$

where Sutherland temperature T_S = 110.4 K, reference viscosity μ_{ref} = 1.719x10^{-5} Pa·s, reference temperature T_{ref} = 273.15 K.

The computations were performed in the CFX 18.0 program, which makes use of the implicit finite volume scheme. Mass, momentum and energy conservation equations were solved:

$$\frac{\partial \rho}{\partial t} + \nabla\left(\rho \boldsymbol{U}\right) = 0 \tag{2}$$

$$\frac{\partial \rho \boldsymbol{U}}{\partial t} + \nabla\cdot\left(\rho \boldsymbol{U}\otimes\boldsymbol{U}\right) = -\nabla \mathrm{p} + \nabla\tau \tag{3}$$

$$\frac{\partial \rho h_{tot}}{\partial t} - \frac{\partial p}{\partial t} + \nabla\cdot\left(\rho \boldsymbol{U} h_{tot}\right) = \nabla\cdot\left(\lambda\nabla \mathrm{T}\right) + \nabla\cdot\left(\mathbf{U}\cdot\tau\right). \tag{4}$$

The conservation equations are Reynolds-averaged, and turbulent stresses are modelled using the Boussinesq hypothesis assuming a stochastic turbulence model for turbulent viscosity determination. Three two-equation turbulence models are adopted in the analyses: RNG k-ε, k-ω SST and SST-SAS. The RNG k-ε model [26, 27] is analysed first. In the standard k-ε model, turbulent viscosity is found based on one turbulence scale, whereas the RNG model takes account of different scales [28]. This is possible due to the application of the renormalization method, which enables gradual elimination of the impact of the smallest scales that cannot be solved using available computer resources.

The second in the analysis is the k-ω SST model [29], which is a combination of the k-ε and the k-ω model. The k-ε model simulates turbulence correctly in the free stream far from the channel wall, but its essential downside is that it inflates the tangential stress values in the boundary layer. For this reason, the flow boundary layer is modelled using the k-ω model, where the transport equation is solved for the turbulent dissipation rate. Beyond the boundary layer, the model is very sensitive to changes in the free stream turbulent dissipation rate ω_f. Depending on ω_f, the turbulent viscosity value may be doubled [30]. For this reason, a blending function is used, which enables a gradual transition from the k-ω model in the boundary layer to the k-ε model as the distance from the wall gets bigger. The k-ω SST model thus ensures correct results in the boundary layer and in the free stream at a relatively low computational cost. This is why this is the most popular turbulence model applied in engineering problems.

The SST-SAS model belongs to the URANS class and takes account of an additional source term in the equation describing the unit rate of energy dissipation ω, which depends on the unsteadiness level. The rise in non-homogeneity is determined using an additional von Kármán scale in this term. The scale is calculated based on the second derivative of velocity [31]:

$$L_{vK} = \kappa\frac{S}{U''} \tag{5}$$

where S – strain rate tensor, U'' – second derivative of velocity, κ – von Kármán constant.

In the case of a non-stationary area, the ratio between the turbulent length and the von Kármán length scales increases, which activates the additional source term Q_{SAS} in the dissipation equation [32]. A rise in dissipation involves a drop in turbulent viscosity, which enables the creation of smaller vortices arising due to decomposition of larger vortex structures. The possibility of modelling these structures is limited by the

numerical mesh and the time step adopted for the calculations. The additional term Q_{SAS} is not active in stationary areas, so the SST-SAS model produces the same results as the standard SST model. Its application is recommended as an alternative to the LES method if unsteadiness is considerable, which is the case here.

2.2 Analysis of the solution sensitivity – k-ω SST turbulence model

The computational area should be discretized taking account of the distribution of flow parameters in the computational domain. Large gradients of parameters require that the numerical mesh density should be selected accordingly. The selection of the mesh for which the obtained solution does not depend on space discretization and the selection of the time step require a sensitivity analysis. The analysis of the solution spatial sensitivity was composed of two stages. First, global parameters of the numerical mesh elements were adopted, and then the boundary layer parameters were selected.

Five numerical meshes were generated, which differed from each other in the number of elements, keeping however appropriate proportions of the element size between different discretization areas. The meshes had 2M, 2.7M, 4.1M, 5.2M and 7.7M elements.

Fig. 3 presents discretization of a fragment of the computational area in the region of the stream supplying the rotor. The mesh smallest elements occur in places with the greatest velocity gradients, i.e. in the upper part of the inter-disc gap and in the entire supply unit. The discretization in the boundary layer area that ensures the value of parameter $y^+ \approx 1$ occurs in the clearance between the rotor tip and the turbine casing, on the walls of the inter-disc gaps and inside the nozzles of the supply unit.

The discretization selection criterion was the turbine power, which – being the most important global parameter – required an appropriately fine mesh in the entire computational domain. Stresses in direction x and y were responsible for the generation of torque for a given spatial orientation of the inter-disc gap computational domain. Power is determined from the following equation:

$$N = \omega_a \int \boldsymbol{r} \times \boldsymbol{\tau} dA \,. \tag{6}$$

This can be expressed as follows:

$$\begin{aligned} \tau_x = {} & n_x\left(\mu+\mu_t\right)2\frac{du}{dx} + n_y\left(\mu+\mu_t\right)\left(\frac{du}{dy}+\frac{dv}{dx}\right) \\ & + n_z\left(\mu+\mu_t\right)\left(\frac{du}{dz}+\frac{dw}{dx}\right) \end{aligned} \tag{7}$$

$$\begin{aligned} \tau_y = {} & n_x\left(\mu+\mu_t\right)\left(\frac{dv}{dx}+\frac{du}{dy}\right) + n_y\left(\mu+\mu_t\right)2\frac{dv}{dy} \\ & + n_z\left(\mu+\mu_t\right)\left(\frac{dv}{dz}+\frac{dw}{dy}\right). \end{aligned} \tag{8}$$

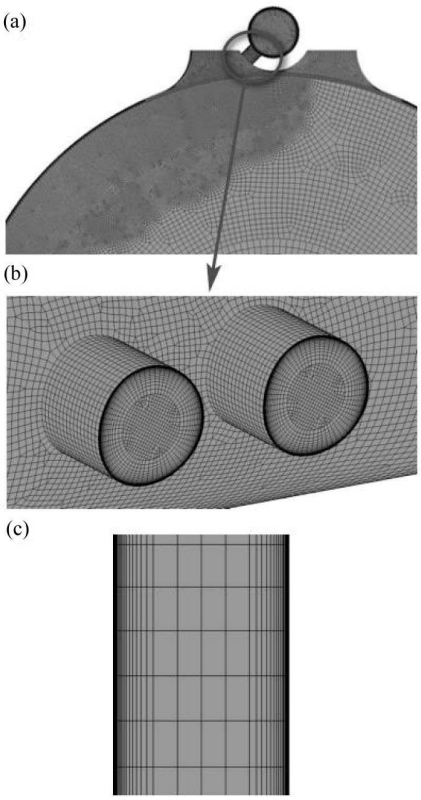

Fig. 3. Domain mesh: (a) General look; (b) inlet orifices; (c) inter-disc gap.

The calculations were performed for the parameters listed in Table 1. Fig. 4 presents a chart illustrating the dependence of power on the number of the mesh elements. The results are presented in relation to the power value obtained from the finest mesh. 3 numerical meshes (4.1M, 5.2M, 7.7M) ensured the calculation accuracy level of 99 %. The mesh composed of ~4.1M elements was selected for further analysis. The length of the element edges in the finer area of inter disc gap was equal to 0.2 mm while in the coarser area was equal to 0.7 mm. The inlet system and the tip clearance domain also consisted of 0.2 mm elements.

The second stage was to select the boundary layer discretization. The variables were: the height of the first element, which had a direct impact on the value of parameter y^+, and the number of layers. The increment in subsequent layers was 1.2, and the boundary layer total thickness was 0.32 mm. Table 2 presents the following parameters: The maximum value of y^+ and the first element height δ_1 of the analysed meshes. Fig. 5 presents relative power related to the reference case as a function of the maximum value of parameter y^+ in the area of the inter-disc gaps.

Mesh 1 was the reference case. It follows from Fig. 5 that meshes 1-4, for which $y^+ < 2$, give similar power values. Compared to power in the reference case, a rise can be observed for cases 2-4 and a considerable drop for mesh 5 and mesh 6. These differences are the direct effect of the accuracy of the determination of the boundary layer velocity profile.

Table 1. Parameters used in the mesh sensitivity analysis.

Inlet	Total pressure	3 bar
	Total temperature	303 K
	Flow direction	Normal to boundary
	Turbulence intensity	5 %
Outlet	Static pressure	1 bar
	Pressure averaging	Avg. over whole outlet
Rotational speed	25000 min^{-1}	
Heat transfer	Total energy	

Table 2. Parameters of the numerical meshes under analysis.

Mesh number	max y^+	δ_1 [mm]
1	0.070	$5 \cdot 10^{-5}$
2	0.15	10^{-4}
3	0.50	$5 \cdot 10^{-4}$
4	1.50	10^{-3}
5	8.00	$5 \cdot 10^{-3}$
6	16.00	10^{-2}

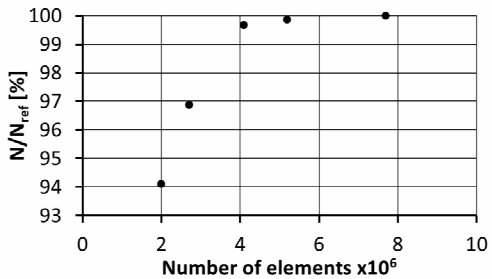

Fig. 4. Analysis of the solution sensitivity to the computational area discretization.

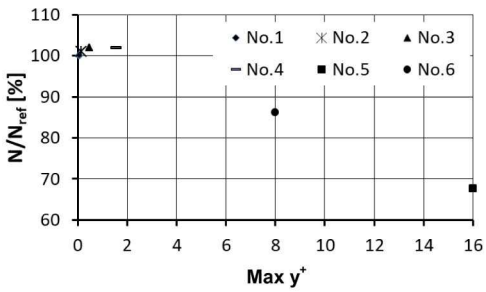

Fig. 5. Boundary layer discretization sensitivity analysis.

For example, Fig. 6 presents changes in non-dimensional velocity u^+ depending on non-dimensional distance y^+ from the wall in the gap between disc 1 and disc 2 in the point with the highest Mach number.

The chart presenting the relation between the two quantities satisfies the law of the wall [33]. According to the theory, for the laminar sublayer of $y^+ < 5$, $u^+ = y^+$, whereas the logarithmic equation $u^+ = 1/k \ln y^+ + C$ holds for the $y^+ > 30$ area

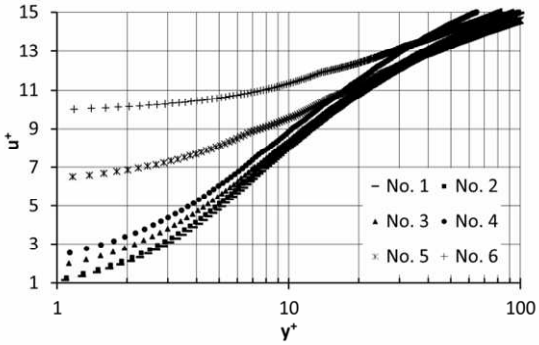

Fig. 6. Non-dimensional velocity u+ as a function of non-dimensional distance from the wall y+ for different numerical meshes.

[34]. For the transitional range of $5 > y^+ > 30$, none of the above relations reflects the correct shape of the profile, but some attempts at finding an appropriate equation can be found in Refs. [35, 36]. It can be seen in Fig. 6 that for meshes 1 and 2 the velocity profile is described exactly according to the $u^+ = y^+$ equation, whereas the profiles for meshes 3 and 4 differ from it only slightly. A further implication of this situation is better accuracy of determination of the velocity gradients, which in turn affect the power value according to Eqs. (6)-(8). For this reason, the turbine power values obtained for meshes 1-4 are at a very similar level. Compared to the reference case, the maximum difference occurs for mesh 4 and totals 2.5 %. In the case of meshes 5 and 6, the accuracy of the velocity profile determination is much worse. It deviates considerably from the law of the wall in the laminar sublayer. Due to that, the tangential stress values are underestimated, which results in respective power values by about 15 % and 30 % smaller than in the reference case. Mesh 3 was selected for further analyses. Finally, after the two sensitivity analyses, the numerical mesh had about 5.1 million elements and 5.22 million nodes. 97 % of elements was hexahedral and the rest were tetrahedral and pyramidal.

In the next stage, the impact of time discretization on the simulation result was also investigated. For this purpose, unsteady-state calculations were performed using a variable time step. The initial time step was selected based on the analysis of the frequency of pressure fluctuations in the supply nozzle. It totalled $\Delta t = 10^{-5}$ s. Next, the time step was doubled, made five times longer, then halved and made four times shorter. The obtained power values related to the reference level as a function of the time step are presented in Fig. 7. It can be noticed that time step $\Delta t = 10^{-5}$ s ensures appropriate time discretization. A further reduction therein does not improve the simulation results significantly. Lengthening the time step involves a difference by about 3.3 %. In view of these results, the time step of $\Delta t = 10^{-5}$ s was selected for further calculations.

2.3 Analysis of the solution sensitivity – SST-SAS turbulence model

A separate sensitivity analysis was conducted for the SAS

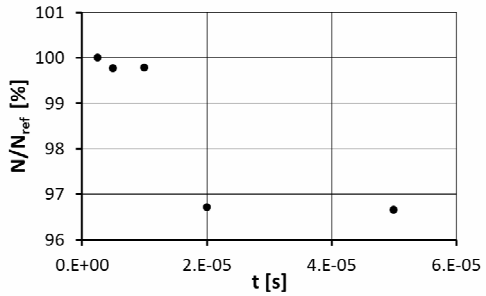

Fig. 7. Analysis of the solution sensitivity to time step Δt.

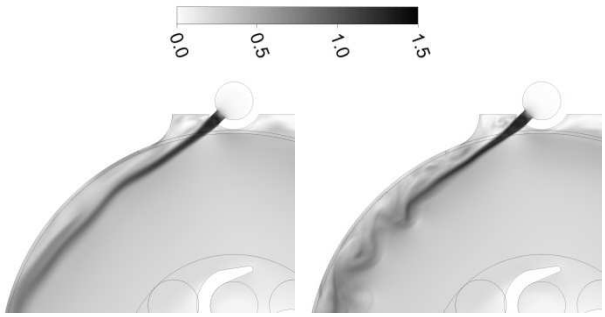

Fig. 8. Mach number distributions for two selected time instants for SASv.1 (top) and the SASv.2 (bottom) models, n = 30000 min^{-1}.

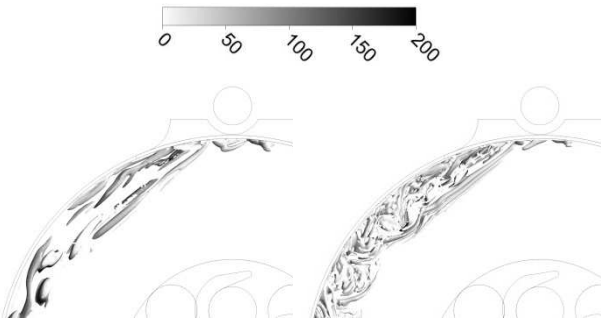

Fig. 9. Q criterion comparison for the SASv.1 (left) and SASv.2 (right) models, n = 30000 min^{-1}.

model. A reduction in the time step and in the size of the numerical mesh elements in this model affects the accuracy of modelling turbulent structures, which may in turn have an effect on the obtained power value [31]. For this reason, an additional analysis was performed to investigate this effect. A mesh was generated with about 12 million elements, with the same proportions of density as the mesh selected for calculations previously. The time step was ten times smaller and totalled $\Delta t = 10^{-6}$ s. The other boundary conditions were identical to those adopted in the previous cases. The mesh with 5.1 million elements is referred to as SASv.1 and the mesh with 12 million elements – as SASv.2.

Fig. 8 presents instantaneous Mach number distribution in the gap between disc 1 and disc 2 for meshes SASv.1 and SASv.2, respectively, and Fig. 9 shows the Q-criterion for Q = $4.5 \cdot 10^8$ s^{-2} with the viscosity ratio contours. Fig. 8 for the SASv.2 case illustrates the process of the jet formation and separation. The jet is straight and cohesive, with distinct boundaries up to about half its length, then it starts to lose its stability. Separation of a part of the jet can be observed. The separated part then proceeds chaotically towards the domain boundary. The jet farther part is characterized by high irregularity and a smaller Mach number. Distinct swirling occurs in the region between the jet and the inter-disc gap boundary. The swirling is characterized by locally increased velocities. Comparing the distributions obtained for the SASv.1 and SASv.2 models, it can be noticed that the mesh density has a significant impact on the flow image. Clear differences can be observed in the velocity distribution in the jet and in the jet shape, whereas the jet width remains the same. In the case of the SASv.1 mesh, the shape is closer to the averaged one and the jet does not lose stability. The swirling area between the jet and the domain boundary is characterized by more regular contours of the Mach number. The jet boundaries can be distinguished clearly along the entire length of the inter-disc gap. In the SASv.1 case, the Mach number inside the jet is slightly lower compared to SASv.2, and its highest values occur only up to about a third of the jet entire length.

In the SASv.2 case, the area with the highest Mach number extends up to the jet half. It follows from Fig. 9 that a finer mesh with a smaller time step makes it possible to take account of smaller non-homogeneities and vortex structures characterized by a higher frequency. This is an effect of lower turbulent viscosity. The turbulent-to-laminar viscosity ratio is presented on the contours of the structures. In the case of the SASv.1 model, the viscosity ratio is higher, which has an effect on the dissipation of smaller-scale vortices. It can be observed that in both cases instances of the greatest unsteadiness occur in the upper part of the inter-disc gap, where velocities are the highest. The finer mesh of the SASv.2 variant makes it possible to model much smaller turbulent structures compared to the SASv.1 model, where the occurrence of only the greatest unsteadiness is made visible. Comparison of time-averaged power obtained from the models proves, that despite the differences in the flow structure, no significant differences in power are observed ($N_{SASv.1}$ = 54.57 W, $N_{SASv.2}$ = 54.08 W). The power value obtained from the SASv.1 model is by 0.49 W higher, and the relative difference is δ_r = 0.76 % only. Considering the much longer computation time and the fact that the only advantage was a more detailed qualitative analysis of the distributions of flow parameters, a decision was made to perform further analyses by means of the SST-SAS model with the SASv.1 mesh.

3. Modelling the turbine power and efficiency characteristics

This section presents selected results of the transient flow field analysis conducted for 3 turbulence models. The turbulence model parameters determine the value of turbulent viscosity, which, as defined by Eqs. (6)-(8), is essential for determination of stresses arising on the surfaces of the discs. The

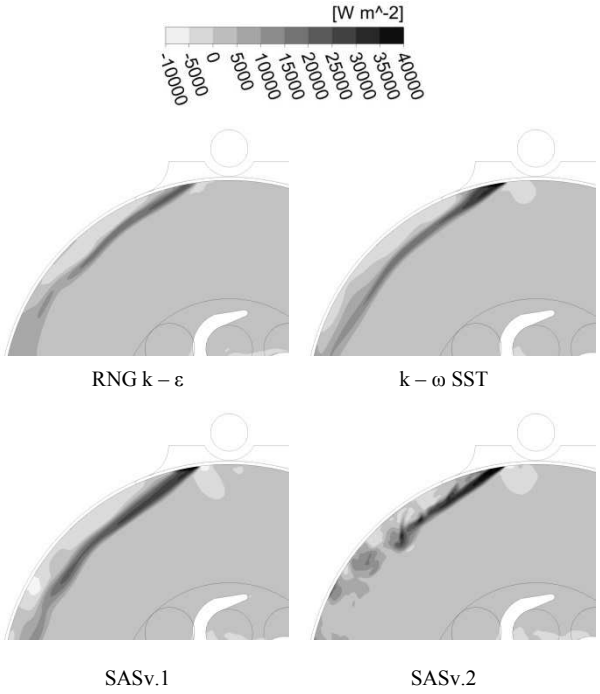

Fig. 10. Contours of instantaneous distributions of power generated on the wall of disc 2, n = 30000 min^{-1}.

stress values determine the moment in relation to the rotor shaft axis and the value of power generated by the turbine. Instantaneous distributions of unit power generated on the surface of disc 2 are shown in Fig. 10. The presented distributions indicate that areas with the greatest power values coincide with areas characterized by the highest velocity gradients. In every case, the highest values are found at the fluid inlet to the inter-disc space. In the case of the RNG k–ε model, they total about N_u = 22.5 kW/m^2; for the other models – N_u = 35 kW/m^2 (k–ω SST), N_u = 37.5 kW/m^2 (SASv.1) and N_u = 42.5 kW/m^2 (SASv.2). Some places can also be distinguished in the figure with negative power reaching up to -10 kW/m^2. They are located in the area between the jet and the disc outer edge. These areas contribute to the decrease in the turbine total power. The power distribution in the jet core is also interesting. In the case of the RNG k–ε model, the values remain practically unchanged on its entire length and drop only by about 5 kW/m^2. In the other cases, the drop is bigger. High power values are maintained in the jet core on its entire length in the case of the SASv.1 and the SASv.2. model. In the other parts of the disc, no essential values of generated power are observed (N_u < 5 kW/m^2). This means that the area which is important in terms of the turbine performance is only the jet flowing directly out of the supply system nozzle.

Considering power optimization, the optimal inflow angle should therefore be selected so that the fluid can move with the highest velocity as far as possible from the shaft axis. Another positive effect will be a reduction in the area of swirling and reverse flows, which can be seen in Fig. 8 between the jet and the inter-disc gap boundary and which slows down the rotor.

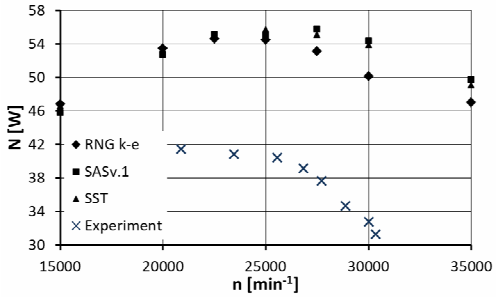

Fig. 11. Characteristic of the turbine power depending on rotational speed.

Curves illustrating changes in the mean power value as a function of rotational speed were plotted for the RNG k–ε, the k–ω SST and the SASv.1 model. They are presented in Fig. 11. It can be observed that each characteristic is parabolic and relatively flat, i.e. power varies only by about 10 % of the maximum value in a wide range of rotational speeds (15000 – 35000 min^{-1}). The highest values of power were obtained for the RNG k–ε model for rotational speed n = 25000 min^{-1}: N = 54.5 W, whereas for the k–ω SST and SASv.1 models – for n = 26000 min^{-1}: N = 55.9 W. For lower rotational speeds, i.e. up to about n = 22500 min^{-1}, the power values for all the cases under analysis are practically the same. A further rise in rotational speed involves a gradually increasing difference between the k-ω SST and SASv.1 models and the RNG k–ε model. It may be concluded that a rise in circumferential and radial velocity involves a reduction in the power value estimated by means of the RNG k–ε model. Power values obtained from experimental investigations are substantially lower compared to ones obtained from numerical analysis. The biggest differences occur for higher rotational velocities (up to 40 %). It should be also noted, that peak values are moved toward lower rotational velocity, to approximately 21000 min^{-1}. It is impossible to assess predictions accuracy of numerical investigations basing on preliminary experiment. A further effort aiming rise of measurement precision level is required. The most important factor affecting the differences is precision of turbine manufacturing. Investigated turbine was just a prototype of demonstrating model. Discs are not ideally parallel to each other after mounting on the shaft, although there is such assumption in CFD analysis. The lack of appropriate sealing in the inlet system also may cause volumetric losses. Apart from that, there is also some level of uncertainty provided by the measurement system. For the SST model, characteristics of efficiency as a function of rotational speed were additionally determined.

The efficiency values were established based on the results obtained from a numerical analysis and by means of theoretical relations [15].

Method 1

Power is determined based on the stress values obtained from the CFD analysis according to the following formula:

$$\eta_i = \frac{N}{\dot{m} c_p T_{in} \left(1 - \left(\frac{p_{out}}{p_{in}} \right)^{\frac{\kappa-1}{\kappa}} \right)}. \quad (9)$$

Because the fluid inlet and outlet parameters were constant, the mass flow was constant for each rotational speed and totalled $\dot{m} = 0.00304$ kg/s.

Method 2

Based on the fluid thermodynamic parameters at the turbine inlet and outlet, the real drop in enthalpy is found and then compared to the isentropic one:

$$\eta_i = \frac{h_1 - h_2}{h_1 - h_{2s}}. \quad (10)$$

Method 3

Method 3 makes use of the approach described by Carey [15]. Isentropic efficiency is defined as:

$$\eta_i = \frac{\left[\left(\widehat{W}_o + 1 \right) - \left(\widehat{W}_i + \xi_i \right) \xi_i \right] (\kappa - 1) M_o^2}{\left(1 - \left(\frac{p_{out}}{p_{in}} \right)^{\frac{\kappa-1}{\kappa}} \right)}. \quad (11)$$

The formula is based on determination of the change in the fluid angular momentum as it flows through the rotor disc. $\hat{W}$ is the non-dimensional relative peripheral speed on the disc biggest radius r_o and on the outlet radius r_i, ξ_i is the ratio between the radii: $r_i/r_o = 0.48$, and M_o – is the Mach number on the disc outer edge. The above quantities can be determined from the following equations:

$$\hat{W}_{i,o} = \left(\frac{v_\theta - U_{i,o}}{U_o} \right) \quad (12)$$

$$\hat{W}_i = \frac{e^{24\xi_i / Re_m^*}}{\xi_i} \left[\frac{Re_m^*}{24} e^{-24\xi_i^2 / Re_m^*} + \left(\widehat{W}_o - \frac{Re_m^*}{24} \right) e^{-24/Re_m^*} \right] \quad (13)$$

$$Re_m^* = \frac{2b}{r_o} \frac{\dot{m}_{1n}}{\pi r_o \mu} \quad (14)$$

$$M_o = \frac{U_0}{\sqrt{\kappa R T}} \quad (15)$$

$$U_o = \omega r_o. \quad (16)$$

It should be noted that the above relations are derived based on assumptions which differ from the conditions adopted in the CFD simulation. The assumptions are compared in Table 3.

Quantity $\widehat{W}_i$ is determined according to Eq. (13), and critical velocity is adopted as circumferential speed on the outer radius.

Table 3. Efficiency calculation assumptions.

Theoretical derivation	CFD analysis
Laminar flow	Turbulent flow
Two-dimensional flow field	Three-dimensional flow field
Non-viscous and incompressible flow, body forces reflect the fluid internal friction	Viscous and compressible flow
Radially symmetric flow field; constant velocity on the outer radius – velocity does not decrease along the streamline	Non-symmetric flow field; velocity decreases on the biggest outer radius along the streamline
Effects due to the pressure gradient along the radius are omitted	Effects due to the pressure gradient are not omitted (e.g. the pressure force acting on the spacer arms)
Critical velocity at the rotor inlet	Velocity higher than critical at the rotor inlet
Homogeneous flow field in every inter-disc gap	Non-homogeneous flow field in inter-disc gaps

Method 4

The method makes use of relation Eq. (12) for the outer radius, but in order to determine non-dimensional circumferential velocity on the biggest radius, mass-averaged velocity found from the distribution determined by means of numerical calculations is assumed, whereas on the smallest radius – the calculations are performed according to Eq. (13).

Method 5

The values of $\hat{W}$ on the inner and outer radius are determined based on Eq. (12), where mass-averaged velocity values found from numerical calculations are substituted.

The efficiency calculation results are presented below. Fig. 12 shows example lines of real and isentropic expansion in the turbine according to Method 2. Line 1-2s illustrates the reversible adiabatic curve and line 1-2 – the irreversible one. The enthalpy at the turbine inlet in point 1 was determined based on static pressure and static temperature. Point 2s was found for constant entropy from point 1 and outlet pressure. Point 2 was determined based on outlet pressure and mass-averaged static temperature at the turbine outlet. The attempt to determine point 2 based on total temperature was abandoned to enable a more detailed comparison of the results obtained by means of different methods. Method 1 takes no account of the exhaust loss and therefore the loss is also omitted in Method 2. The results obtained from Methods 3-5 are listed in Tables 4 and 5, respectively. The modified Reynolds number was determined assuming average dynamic viscosity in the gap, and critical velocity v_0^* was calculated for the static parameters listed in Table 1. The mass flow through one supply nozzle reached the critical value for the pressure ratio under consideration upstream and downstream the nozzle. For this reason, it was constant for every rotational speed and totalled $m_{1n} = 0.00152$ kg/s.

Fig. 13 presents characteristics obtained by means of the

Table 4. Efficiency determined by means of Method 3.

n [min^{-1}]	$v^*_{\theta o}$ [m/s]	Re^*_m	M_0	W_i	W_o	η_i [%]
15000	348.92	60.536	0.164	9.201	5.086	5.8
20000	348.92	60.882	0.219	6.873	3.564	7.4
22500	348.92	60.980	0.246	6.095	3.057	8.2
25000	348.92	61.118	0.274	5.473	2.651	8.9
27500	348.92	61.264	0.301	4.964	2.320	9.6
30000	348.92	61.370	0.329	4.540	2.043	10.2
35000	348.92	61.249	0.383	3.867	1.608	11.4

Table 5. Efficiency determined by means of Methods 4 and 5.

n [min^{-1}]	$v_{\theta o}$ [m/s]	W_o	Method 4		Method 5		
			W_i	η_i [%]	$v_{\theta i}$ [m/s]	W_i	η_i [%]
15000	332.8	5.81	11.11	4.1	63.8	0.63	20.7
20000	298.6	3.91	7.96	5.1	73.6	0.48	26.1
22500	358.5	4.17	8.40	6.8	77.9	0.43	35.2
25000	346.3	3.62	7.49	7.4	82.9	0.39	38.6
27500	305.7	2.91	6.30	7.3	87.3	0.35	45
30000	407.7	3.56	7.38	10.4	95.3	0.35	54.9
35000	405.4	3.03	6.50	12.3	101.4	0.28	65.9

methods described above. It follows from Fig. 13 that Methods 1-4 give similar efficiency values. The results obtained from Methods 1 and 2 are identical up to the rotational speed of 25000 min^{-1}, and the maximum is achieved for n = 23000 min^{-1}.

It should be noted that the characteristics obtained from formulae (11-16) (Methods 3-5) are linear, which makes it impossible to predict the theoretical maximum efficiency that could be achieved for given parameters of the fluid and a given geometrical configuration of the turbine. Analysing the velocity values on the rotor outer radius, it may be stated that the assumption adopted in Method 3 of constant critical velocity at the rotor inlet may be burdened with the maximum error of about 15 %. Nonetheless, the assumption can be realized at a greater number of supply nozzles on the perimeter.

Despite increased precision of the velocity determination, the efficiency characteristic obtained by means of this method differs more from the characteristics obtained based on power calculations from stresses on the surface of the discs and from the enthalpy drop (Method 1 and Method 2, respectively) than the characteristic determined by means of Method 3. The difference between the characteristics found using Method 3 and Method 4 proves a significant impact of the flow field non-homogeneity. Method 5 determines efficiency based on a transformed Euler turbine equation for distributions obtained from the numerical analysis. However, the method takes no account of the streamline shape or length and omits the flow phenomena arising along the flow path as well as the jet unsteadiness and direction. Therefore, it may be concluded that

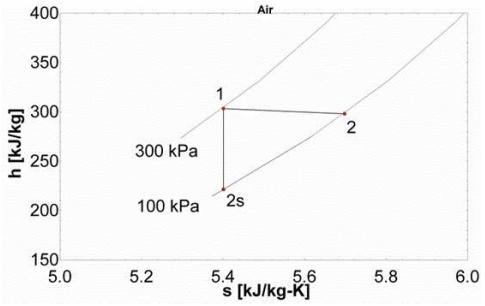

Fig. 12. Example lines of real and isentropic expansion in the Tesla turbine.

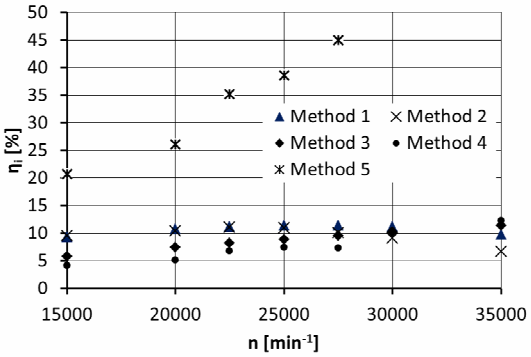

Fig. 13. Tesla turbine efficiency characteristics found using different methods.

efficiency in this case concerns the maximum efficiency of the rotor that can be achieved at the fluid certain kinematic parameters rather than the turbine real efficiency. The method does not take account of the change in the fluid direction due to the outlet structure, which may cause additional losses.

4. Summary and conclusions

This paper presents the results of the Tesla turbine numerical analysis performed for different turbulence models: the RNG k–ε, the k–ω SST and the SAS model. The analysed model reflected the geometry of an existing turbine with the rotor diameter of 73 mm and with 5 discs. The time and space discretization sensitivity analysis was conducted. Qualitative and quantitative differences obtained from the SAS model with a thicker and thinner mesh, as well as with a smaller and bigger time step, were indicated. The SAS model with a thicker mesh and a smaller time step took account of smaller vortex structures and more instances of unsteadiness. This, however, did not translate into a great improvement in the power estimation by means of the numerical analysis. The highest unit power on the rotor discs was obtained for the SAS model with a more precise discretization, whereas the RNG k–ε model gave the smallest values. The area between the jet and the inter-disc gap boundary was characterized by swirling and reverse flows, which slowed the rotor down. Comparing the characteristics of power as a function of rotational speed, it

may be concluded that the SAS model with a thinner discretization and the k–ω SST model predict similar power values. For higher rotational speeds, the RNG k–ε model predicts lower values compared to the other models. The turbine efficiency was estimated using 5 methods. The methods based on the determination of the drop in enthalpy, power from stresses arising in the fluid and on the theoretical relations developed by Carey produced similar results.

The analysis presented in this paper makes it possible to assess the methods of determination of the Tesla turbine operating parameters in terms of their usefulness for establishing the turbine potential for practical applications.

Acknowledgments

The presented work was performed within the Silesian University of Technology statutory research funds for young scientists. This research was partially supported by the PL-Grid Infrastructure.

Nomenclature

b	: Inter-disc gap
c_p	: Specific heat at constant pressure
h	: Specific enthalpy
L_{vK}	: von Kármán scale
M	: Torque
M_0	: Mach number on the disc outer edge
m_{1n}	: Mass flow from one nozzle
N	: Power
N_u	: Unit power
n_i	: Normal vector in direction i
n	: Rotational speed
R	: Gas constant
Q	: Q-criterion
r	: Radius
Re_m^*	: Modified Reynolds number
s	: Specific entropy
T	: Temperature
T_s	: Sutherland temperature
t	: Time step
u	: Tangential velocity
u^+	: Non-dimensional velocity
v_θ	: Peripheral velocity
W	: Non-dimensional relative peripheral velocity
y^+	: Non-dimensional distance
δ_1	: Height of first boundary layer element
δ_r	: Relative difference
η	: Efficiency
κ	: von Kármán constant
μ	: Laminar viscosity
μ_t	: Turbulent viscosity
ρ	: Density
τ	: Tangential stress
ω_a	: Angular velocity

References

[1] N. Tesla, Turbine, *Patent No: 1,061,206*, United States Patent Office of New York (1913).

[2] The Tesla steam turbine, The rotary heat motor reduced to its simplest terms, *Scientific America*, 30 September (1911) 296-297.

[3] T. Engin, M. Oezdemir and S. Cesmeci, Design, testing and two-dimensional flow modelling of a multiple disk fan, *Experimental Thermal Fluid Science,* 33 (8) (2009) 1180-1187.

[4] W. Rice, Tesla turbomachinery, *IV International Tesla Symposium*, Belgrade, Yugoslavia (1991) 117-125.

[5] A. L. Neckel and M. Godinho, Influence of geometry on the efficiency of convergent – divergent nozzles applied to Tesla turbines, *Experimental Thermal and Fluid Science,* 62 (2015) 131-140.

[6] X. L. Tong and E. Luke, Turbulence models and heat transfer in nozzle flows, *AIAA*, 42 (11) (2004) 2391-2393.

[7] K. Rusin and W. Wróblewski, Numerical analysis of the Tesla turbine operating conditions, *Współczesne Problem Energetyki*, 4 (2017) 97-106.

[8] K. Rusin, The influence of outlet system geometry on Tesla turbine working parameters, *Acta Innovations*, 22 (2017) 58-67.

[9] S. Sengupta and A. Guha, A theory of Tesla disc turbines, *Journal of Power and Energy,* 226 (5) (2012) 650-663.

[10] P. Lampart and Ł. Jędrzejewski, Investigations of aerodynamics of Tesla bladeless turbine, *Journal of Theoretical and Applied Mechanics,* 49 (2) (2011) 477-499.

[11] C. K. Kim and J. Y. Yoon, Performance analysis of bladeless jet propulsion micro steam turbine for micro-CHP (combined heat and power) system utilizing low-grade heat sources, *Energy*, 101 (2016) 411-420.

[12] F. Hamdi, J. Seo and S. Han, Numerical investigation of an organic Rankine cycle radial inflow two-stage turbine, *Journal of Mechanical Science and Technology,* 31 (4) (2017) 1721-1728.

[13] E. Yun, H. Park, S. Y. Yoon and K. C. Kim, Dual parallel organic rankine cycle (ORC) system for high efficiency waste heat recovery in marine application, *Journal of Mechanical Science and Technology,* 29 (6) (2015) 2517-2528.

[14] S. Yatsuzuka, Y. Niiyama, K. Fukuda, K. Muramatsu and K. Shikazono, Experimental and numerical evaluation of liquid-piston steam engine, *Energy,* 87 (2015) 1-9.

[15] V. P. Carey, Assessment of Tesla turbine performance for small scale Rankine combined heat and power systems, *Journal of Engineering for Gas Turbines and Power*, 132 (2010) 122301-1 – 122301-8.

[16] P. Lampart, K. Kosowski, M. Piwowarski and Ł. Jędrzejewski, Design analysis of Tesla micro-turbine operating on a low-boiling medium, *Polish Martime Research*, 63 (16) (2009) 28-33.

[17] J. Song, C. Gu and X. Li, Performance estimation of Tesla turbine applied in small scale organic rankine cycle (ORC) system, *Applied Thermal Engineering,* 110 (2017) 318-326.

[18] G. E. Miller, B. D. Etter and J. M. Dorsi, A multiple disk pump as a blood flow device, *IEEE Transactions on Biomedical Engineering*, 37 (2) (1990) 157-163.
[19] Ł. Szablowski, P. Krawczyk, K. Badyda, S. Karellas, E. Kakaras and W. Bujalski, Energy and exergy analysis of adiabatic compressed air Energy storage system, *Energy*, 138 (2017) 12-18.
[20] S. Kapila, A. O. Oni and A. Kumara, The development of techno-economic models for large scale energy storage systems, *Energy,* 140 (1) (2017) 656-672.
[21] W. M. J. Cairns, *The Tesla disc turbine*, Camden Miniature Steam Service, Great Britain (2003).
[22] G. P. Hoya and A. Guha, The design of a test rig and study of the performance and efficiency of a Tesla disc turbine, *Journal of Power and Energy,* 223 (4) (2009) 451-465.
[23] A. Guha and B. Smiley, Experiment and analysis for an improved design of the inlet and nozzle in Tesla disc turbine, *Proc. IMechE Part A: J Power Energy*, 224 (2) (2010) 261-277.
[24] R. Li, H. Wang, E. Yao, M. Li and W. Nan, Experimental study on bladeless turbine using incompressible working medium, *Advances in Mechanical Engineering*, 9 (1) (2017) 1-12.
[25] W. Sutherland, The viscosity of gases and molecular force, *Philosophical Magazine,* 5 (36) (1893) 507-531.
[26] V. Yakhot, S. A. Orszag, S. Thangam, T. B. Gatski and C. G. Speziale, Development of turbulence models for shear flows by a double expansion technique, *Physics of Fluids A: Fluid Dynamics,* 4 (1992) 1510-1520.
[27] V. Yakhot and L. M. Smith, The renormalization group analysis of turbulence. I. Basic theory, *Journal of Scientific Computing,* 1 (1) (1986) 3-51.
[28] S. E. Ghasemi and A. A. Ranjbar, Numerical thermal study on effect of porous rings on performance of solar parabolic trough collector, *Applied Thermal Engineering,* 118 (2017) 807-816.
[29] F. R. Menter, Zonal two equation k-ω turbulence models for aerodynamic flows, *24th Fluid Dynamics Conference,* Orlando, USA (1993).
[30] F. R. Menter Influence of freestream values on k-ω turbulence model predictions, *AIAA Journal,* 30 (6) (1992) 1657-1659.
[31] F. Menter and Y. Egorov, The scale-adaptive simulation method for unsteady turbulent flow predictions, *Flow, Turbulence and Combustion,* 85 (1) (2011) 113-138.
[32] L. Davidsion, Evaluation of the SST-SAS model, channel flow, asymmetric diffuser and axial-symmetric hill, *Proc. European Conference on Computational Fluid Dynamics,* Delft, The Netherlands (2006).
[33] T. von Kármán, Mechanische Ähnlichkeit und Turbulenz, Nachrichten von der Gesellschaft der Wissenschaften zu Göttingen, *Fachgruppe 1 (Mathematik)*, 5 (1930) 58-76.
[34] H. Schlichting, *Boundary-layer theory,* Seventh Ed., McGraw-Hill Book Company, New York, USA (1979).
[35] I. Wygnanski, Y. Katz and E. Horev, On the applicability of various scaling laws to the turbulent wall jet, *Jurnal of Fluid Mechanics,* 234 (1992) 669-690.
[36] W. K. George and L. Castillo, Zero pressure gradient turbulent layer, *Applied Mechanics Reviews,* 50 (1997) 689-729.

Krzysztof Rusin, M.Sc., is a Ph.D. student in the Institute of Power Engineering and Turbomachinery at Silesian University of at Technology. His research interests include turbo-machinery, CFD methods and fluid dynamics.

Włodzimierz Wróblewski completed his Ph.D. in 1989 and was awarded Dr.Sc. in 2001 at Silesian University of Technology in Gliwice. He is now a Professor in the Institute of Power Engineering and Turbomachinery, Sile-sian University of Technology. He is a Head of Division of Turbomachinery and Power Systems. His research fields are fluid mechanics, heat transfer and power plant systems. He has been involved in the projects related to the power plant systems simulations, flow field modelling in turbomachinery, conjugate heat transfer in turbine blades, numerical modelling of two-phase flows with condensation and with cavitation.

Sebastian Rulik, Ph.D., works in the Institute of Power Engineering and Turbomachinery at Silesian University of Technology. His main field of interest are CFD methods, optimization algorithms and development of new cooling techniques dedicated for turbomachinery applications.